CrossMark

3D crustal structure of the northwest Alborz region (Iran) from local earthquake tomography

M. Rezaeifar[1,4] · E. Kissling[1] · Z. H. Shomali[2,3] · M. Shahpasand-Zadeh[4]

Abstract We performed a 3D seismic tomography study of the northwest Alborz region in Iran, by inversion of P-wave arrival times of nearly 250 local earthquakes recorded at 13 permanent stations between 2006 and 2010. We applied the simultaneous inversion code SIMULPS14 carefully tuned to data set by choice of optimal regularization parameters. Resolution tests with synthetic data show that the inversion results are well constrained around the North Tabriz Fault (NTF) from 3 to 16 km depth. In this depth range, our results show a series of anomalies with relatively high and low velocity, reflecting the heterogeneous geology of northwest Alborz and generally correlating well with local changes of rock types at the surface across this section of the NTF. The boundary surface between the distinct velocity anomalies is generally consistent with the NTF strike. The high and low velocity anomalies at 5–14 km depth parallel to the surface expression of the NTF are interpreted as basaltic volcanic rocks in the south and Mesozoic sedimentary and basement rocks in the north. In addition, cross sections show a significant change in dip of the NTF in the southeastern part, from nearly vertical in the NW to about 60° dip toward SE.

✉ M. Rezaeifar
meysam.rezaeifar@erdw.ethz.ch; mhmr20@gmail.com

1   Department of Geophysics, ETH Zurich, Institut für Geophysik, Sonneggstrasse 5, 8092 Zurich, Switzerland

2   Institute of Geophysics, University of Tehran, Tehran, Iran

3   Department of Earth Sciences, Uppsala University, Uppsala, Sweden

4   Department of Geology, Graduate University of Advanced Technology, Kerman, Iran

1 Introduction

The northwest Alborz region and easternmost Turkey are parts of the Alpine-Himalayan orogenic belt with a high level of seismicity in a local transpressional tectonic regime. This region constitutes the Arabia-Eurasia continental collision zone, which is located between two thrust belts, the Caucasus to the north and the Zagros Mountains to the south (Fig. 1; Copley and Jackson 2006; Hessami et al. 2003).

Based on GPS measurements and earthquake focal mechanisms, the Arabia-Eurasia convergence has been accommodated mainly through right-lateral N- to NW trending strike-slip faulting in the Alborz region and the SE Turkey (Fig. 1; Djamour et al. 2011; Rastbood and Voosoghi 2011). In eastern Turkey, the North Anatolian Fault (NAF) accommodates slip between Eurasia and Anatolia over a length of >1200 km (Fig. 1; Jackson 1992; Westaway 1990, 1994). Right-lateral fault systems in the eastern Turkey-NW Alborz region, however, seem to become more discontinuous, consisting of several apparently separated fault segments (Fig. 1). The North Tabriz Fault (NTF) constitutes a part of this extensive and complex fault system which partially transfers the motion across the North Anatolian and East Anatolian faults motion to the east, namely toward the Alborz and the Zagros mountain belts of Iran (Moradi et al. 2011). Catastrophic historical earthquakes associated with ruptures along the NTF not only destroyed cities and many villages in the Tabriz region but also inflicted heavy damage on Tabriz Capital. Though the historical seismicity has been linked to repeated rupturing
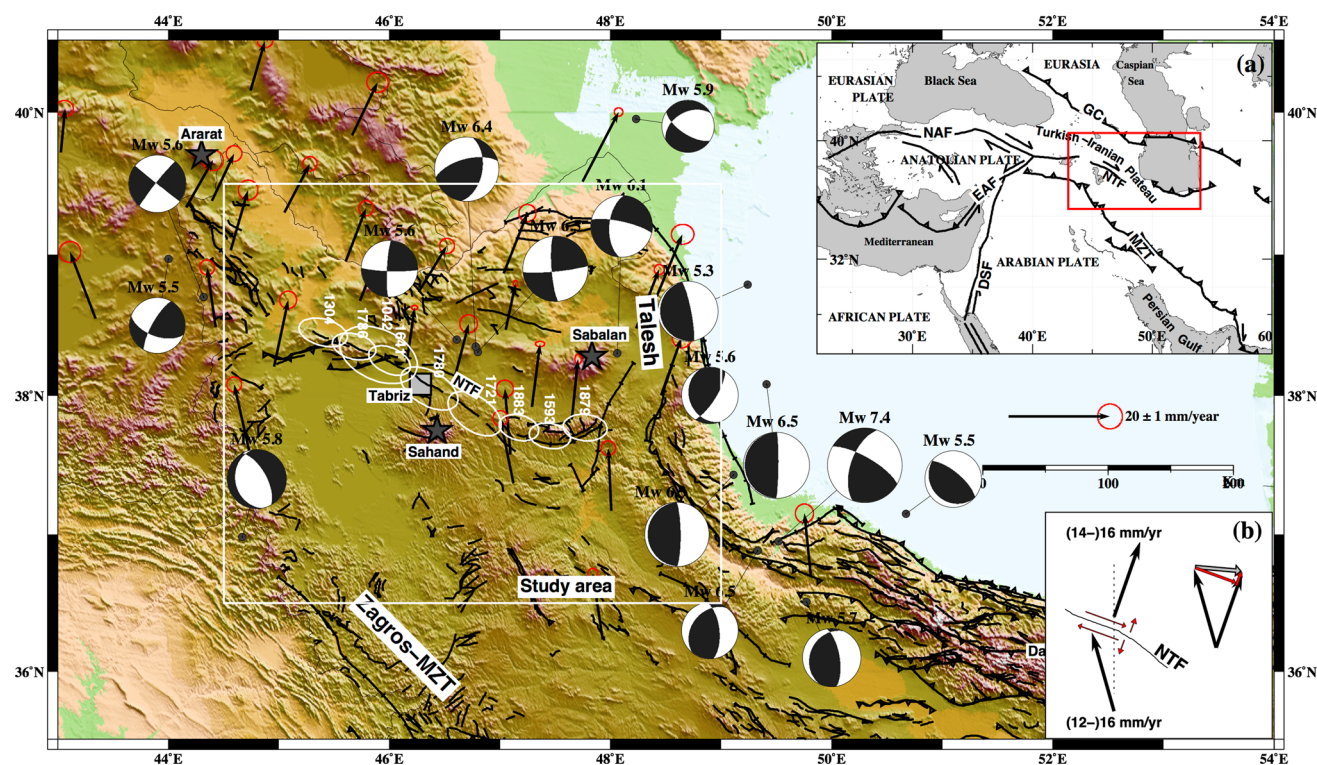
Fig. 1 Summary seismotectonic map of NW Iran. Major active faults are shown as *solid black lines*. *Arrows* and *red uncertainty ellipses* are GPS measurements (Rastbood and Voosoghi 2011). *Gray stars* display the location of volcanoes related to collision between the Arabia and Eurasia (Kheirkhah et al. 2009). The *square* shows location of Tabriz city. The *white ellipses* show the potential location of historical events on the North Tabriz Fault (NTF). Fault plane solutions are from the Global Centroid-Moment-Tensor (CMT) catalogue (http://www.globalcmt.org/). The *white box* in Fig. 1 illustrates the study area (Fig. 2). *Upper right inset* (Fig. 1a) shows the geodynamic setting of the Arabia-Eurasia collision/subduction framework while the *lower right inset* (Fig. 1b) shows the average velocity vectors on both northern and southern side of the NTF. Based on the GPS data it can be noted that, considering a 12 mm/year velocity vector for the southern side of the fault compared to 14 mm/year for the northern side, a locally transtensional tectonic regime will result for the NTF

of different segments of the NTF in the past (e.g., the 858, 1042, 1273, 1304, 1550, 1641, 1717, 1721, 1780 and 1786 earthquakes; Fig. 1; Ambraseys and Melville 1982; Berberian 1997; Rizza et al. 2013), it has not been seismically very active during most of the last 200 years. Furthermore, it seems there are much longer periods of quietism along the southeastern segment of the NTF, which is in the focus of this study, in comparison to the other segments. On the other hand, along this segment, a good part of the strain might be accommodated aseismically, or alternatively, there could be additional and so far undetected small fault segments that accommodate some strain. With its historical seismic record, the NTF is considered as one of the most active faults with a clear surface expression in NW Iran. It has an average strike of NW–SE over a length of about 150 km and an apparently near-vertical dip. Exact location, orientation and dip of the fault segments in many places, however, still remain under debate, depth information is almost completely missing (Berberian 1976; Copley and Jackson 2006; Hessami et al. 2003). Although the NTF seems to represent a linear transform fault, significant local

normal and/or thrust components have also been observed on a few CMT solutions along different segments of the fault (Copley and Jackson 2006). Moradi et al. (2011) suggested that these components of seismic mechanisms could be explained either by extension between the NTF and the Talesh block or a combination of strike slip and reverse faulting at the NTF terminations.

The tectonic complexity in the Albroz region is enhanced by past (post ~10 Ma) and recent volcanism, ranging from a basaltic to rhyolitic affinity (Kheirkhah et al. 2009). These volcanoes constitute part of a vast magmatic province that stretches from eastern Iran across central and western Anatolia (Kheirkhah et al. 2009) within the Arabia–Eurasia collision zone (Fig. 1). Kheirkhah et al. (2009) suggested that strike slip faulting and related pull-apart basins control such volcanic activity in the Alborz region. In NW Iran, however, no clear evidence has yet been provided for such a relationship between volcanic activity and faulting along the NTF.

Finally, different modes of faulting have been proposed for the southern section of the NTF and, in particular, its
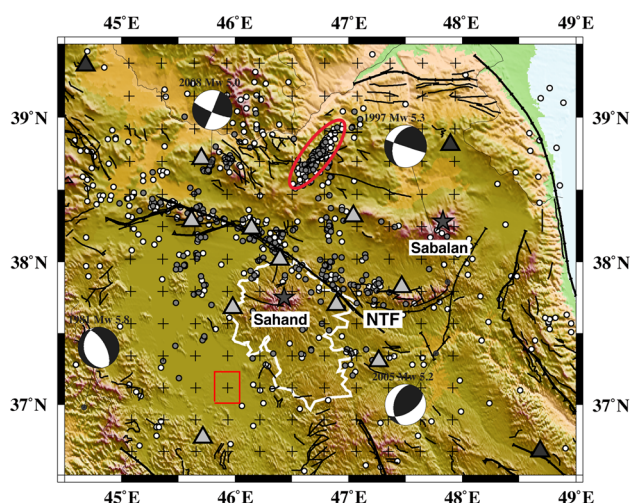
Fig. 2 This map of NW Alborz region shows IRSC stations (*light gray triangular*) and IIEES stations (dark *gray triangular*). *White circles* indicate all 1155 earthquakes reported in the period 2006–2010 and *gray circles* show the 750 earthquakes selected (to read the selection criteria, see the text) for local tomography; *gray stars* Sahand and Sabalan volcanoes, *thin black lines* main faults in the region, North Tabriz Fault (NTF). *Horizontal node* (crosses) spacing for the 3D model is 25 km. *Red box* shows the inversion cell size. *White polygon* illustrates the border of volcanic rocks around Sahand volcano based on the geology map (Haghipur and Aghanabati 1985). *Red ellipse* shows possible cluster of explosions. Fault plane solutions of large events (Mw >5.0) are from the global CMT catalogue (http://www.globalcmt.org/)

southern end where it possibly splits up into different branches (Fig. 1). Based on fault plane solutions, Moradi et al. (2011) documented the NTF as a strike slip fault system with reverse faulting at either end. Azizi and Moinevaziri (2009) on the other hond, based on geochemistry and tectonic considerations, suggested a predominant thrust component for the NTF.

Without clear information about the 3D structure down to a mid-crustal level, possible relationships between the NTF and the above mentioned volcano-tectonic activity cannot be addressed, nor can the seismo-tectonic issues be discussed. Of particular interest are the local variations of the NTF fault segment orientation and the dip of these segments at depth and also their relation to the local 3D upper-crustal structures (Bayramnejad 2007). In this paper, we document the results of a local earthquake seismic tomography, focusing on the upper crustal structure of the NTF in the Alborz region of NW Iran (Fig. 1).

2 Local earthquake data and methodology

The data used in this study are P-wave arrival times from local earthquakes recorded during the period of February 2006 to October 2010 by nine short-period and four broadband permanent stations administrated by Iranian

Seismic Telemetry Network (IRSC) and Iranian Broadband Seismic Network (IIEES) (Figs. 2, 3). From a total of 1155 routinely located events by one or both networks within our study region (Fig. 2), 750 events have been selected by the criteria of azimuthal gap ≤270 and RMS residual less than 1.0 s. For these 750 events, we merged the observations from the two networks and relocated all of them with the Bayramnejad (2007) 1D velocity model. This data set includes a significant number of explosions (recognized as being shot regularly at 9:30 UTC) in a specific spatial cluster marked with a red ellipse in Fig. 2 (Moradi et al. 2011). If we restrict the gap to 180° and select the events with the number of observations larger than 6, as is required for 3D tomography, we obtain 251 events and 1589 observations with a good ray coverage in the immediate vicinity of the NTF (Fig. 3).

The final data set of 1598 routinely picked P travel time were used to: (1) develop a so-called minimum 1D velocity model (Kissling et al. 1994) for the study area, and (2) to perform a simultaneous inversion for 3D tomography velocity structures. To calculate the minimum 1D velocity model, we used the program code VELEST (Kissling et al. 1995), and the Bayramnejad (2007) velocity model as an initial reference model. To explore the model solution space, we performed a series of inversions with different initial models (Kissling et al. 1995). The results of these tests document fast convergence to our final 1D velocity model (Fig. 4).

We obtained a 1D model for the study region that shows a relatively simple crustal structure with a surface layer of about 5 km thickness and a P velocity of 5.1 km/s over an anomalously thick (23 km) upper crustal layer with a velocity of about 6.1 km/s (Fig. 4). Our results further suggest a pronounced Conrad discontinuity with lower crustal velocities of about 6.6 km/s below. Due to the depth distribution of hypocenters (Fig. 3) and the limited lateral extent of the study region the lowermost crustal velocity and the Moho depth are poorly resolved.

The two networks report an average overall observation error of less than 0.4 s for the data. This corresponds well with our findings from VELEST inversions where we observe an initial RMS of 0.6 s and a final RMS of 0.2 s for the minimum 1D model with station corrections.

To study the 3D velocity structures, we applied the well-known simultaneous inversion code SIMULPS14 (Eberhart-Phillips 1993; Evans et al. 1994; Thurber 1993), extended by a full 3D ray shooting technique (Haslinger and Kissling 2001). Since SIMULPS14 solves the non-linear, coupled hypocenter-velocity problem by a linearized, iterative, damped, least-square approach, the solution depends on the initial model parameters such as velocities and hypocenters, damping values, and in particular, on model parameterization (see Kissling et al.

Fig. 3 Location of 750 primary selected local events (*gray dots*) after relocating with our 1D velocity model. The *blue dots* indicate the location of 251 final selected events to perform 3D tomography (see text regarding the selection criteria). *Gray triangles* and crosses show station location locations and positions of grid nodes in the study area, respectively. *Horizontal ray* coverage of the data set is depicted in *black solid lines* between the earthquake epicenter and stations. Two sections along latitude and longitude portray hypocenter distribution by depth. The histogram demonstrates earthquakes depth distribution for primary selected (*gray*) and final selected (*blue*) data sets. Note the vertical exaggeration factor of 5 in the cross sections
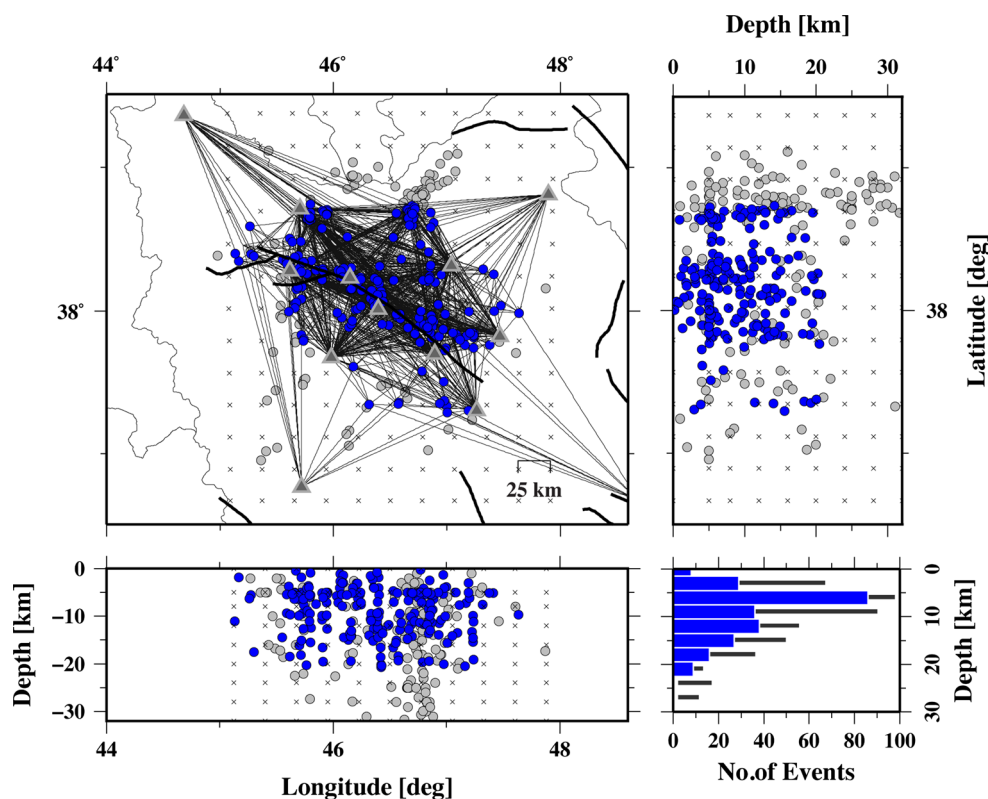
2001). SIMULPS14 includes a combined seismic-inversion grid (representing the 3D velocity structure), locally updated with a finer grid for best performance of 3D shooting ray-tracer. Seismic velocities are linearly interpolated between grid nodes. After testing different grid sizes and considering the ray distribution of the selected data, a horizontal grid with 25×25 km node spacing covering an area of 250×300 km was chosen for the inversion (Figs. 2, 3). Vertical grid spacing (0.0, 5.0, 8.0, 12.0 and 16.0) based on the layering of the preferred 1D model, as a result of inversion with VELEST, was used as an initial velocity model for the 3D inversion (Fig. 4).

Using the approach of Eberhart-Phillips (1986), a series of three-iteration inversions was performed, to establish the trade-off curve between data variance and model complexity with damping values ranging from 30 to 1000 (Fig. 5a). Based on the observation error of our data set and the choice of inversion gridding, damping values between 70 and 300 seem to yield reasonable results. To find the optimum damping value, we used synthetic testing (Kissling 1988). Figure 5b illustrates the recovered models for the 12 km depth plane obtained with the three different damping values 70, 150 and 500. Obviously, the solution is strongly over-damped with a damping value of 500 (compare amplitudes of anomalies for results with different damping shown in Fig. 5b). Conversely, for a low damping value of 70, the region of the recovered model is

significantly larger, but the results include artifacts that prevent reliable interpretation. Hence, considering the probable location of strongest bending in the trade-off curve (Eberhart-Phillips 1986) and considering the results of synthetic testing (Fig. 5), a damping value of 150 with three iterations has been chosen as most appropriate for the inverse problem at hand.

3 Resolution analysis

In order to evaluate the resolving power of the data set and to examine model resolution, we investigated various standard measures such as derivative weighted sum (DWS), and resolution diagonal elements (RDE) (see Fig. 6a, b). DWS is an estimate of total ray length affecting a model parameter and, hence, a more appropriate measure of ray coverage by the data when compared to simple hit counts (HIT). RDE is yet a better estimate of the model resolution for each node, since it incorporates also directional coverage by rays (Kissling 1988). In an ideal situation, a zero value of RDE implies no resolution, while 1 stands for perfect resolution (Toomey and Foulger 1989). For any inverse problem, the resolution quality for specific RDE values may be obtained by synthetic data testing.

The tomographic results show a pronounced lateral velocity variation in the upper crust between about 3 and
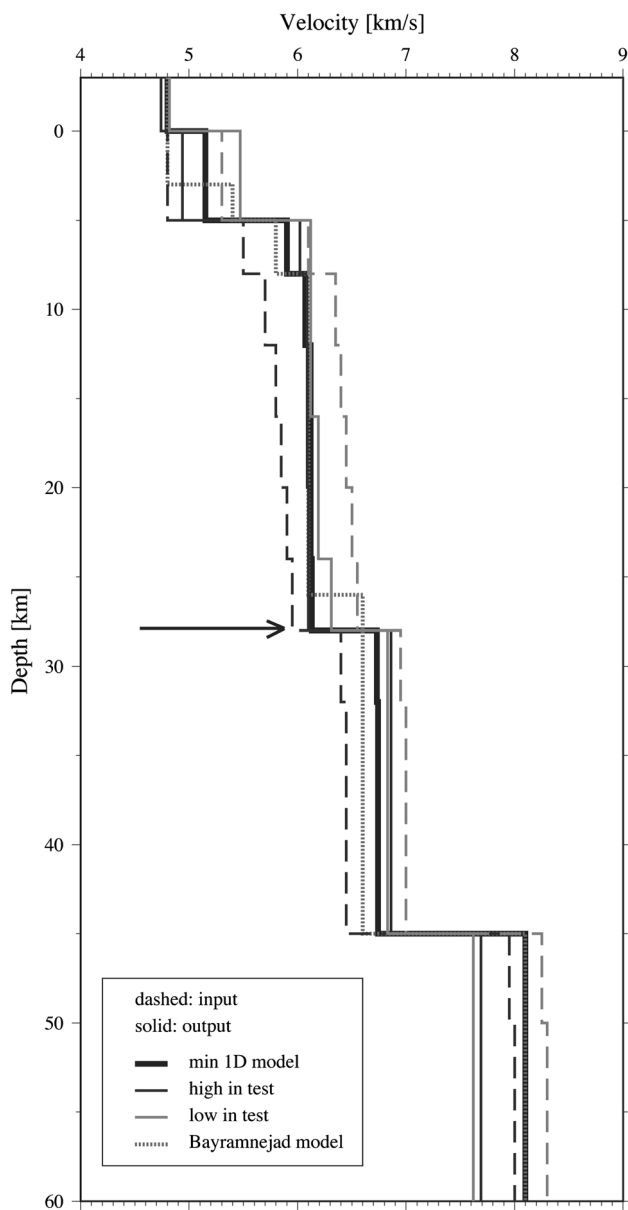
Fig. 4 The *thick solid line* shows the achieved 1D P-wave velocity model, which was used in this study as the starting velocity model for tomography inversion. The *dashed lines* denote all input models to perform stability tests and *thin solid lines* show corresponding output models. *Dotted line* shows the Bayramnejad (2007) model, used as one of our initial testing models for VELEST inversion. The Moho depth at 45 km is inferred from Taghizadeh-Farahmand et al. (2010) who documented depth variation from 38 km in west to 53 km in the eastern part of study area. *Arrow* shows the Conrad discontinuity between the upper and lower crust

14 km depth (Fig. 6c). To assess resolution capabilities and to better understand reliability of the velocity anomalies in this region, following Husen et al. (2000), we performed some characteristic (synthetic) data tests. Based on the apparent shape and location of the anomalies, two synthetic 3D models were constructed. The models consist of two large-amplitude (±5 %) high and low velocity anomalies relative to the 1D initial velocity model, in one case parallel and in another perpendicular to the NTF fault strand (Fig. 7a, b). The source-station pairs of the real data set were used to calculate synthetic travel times within the model volume and a Gaussian distributed error of 0.5 s was added to account for the observation errors in the real data set. The synthetic data set is then inverted by using the same procedure as for the real data. In order to analyze the resolution, we compare the recovered model with the known synthetic models. The results of the synthetic test in Fig. 7a, b indicate an acceptable resolution around the NTF, in the central part of the model, for depths below 6 km, whereas the resolved area below 14 km depth is very small. In the depth range from surface to 6 km (see depth section 5 km in Fig. 6c), however, the image may be locally influenced by artifact anomalies resulting from vertical leakage of deeper layers and/or local near-surface effects and possibly from data errors. Comparison of the resolution of recovered anomalies for both cases and distribution of the RDE values document that the area with RDE values larger than 0.1 can be considered as a region where structures of minimum 40 km length and of velocity anomalies of 2 % and more are very reliably imaged. Subsequently, we refer to this area as the region of highest resolution.

Between the depths of 6–14 km inside the well-resolved area (Fig. 6c), the boundary between the two extensive anomalies follows the NTF trend. In the uppermost layer, however, the high velocity anomaly clearly reaches across the fault line and overlays the low velocity anomaly. To test if these specific results are well resolved and reliable, we performed two further tests evaluating parameterization of our inversion process (Figs. 7c, d). First we put an east–west 4 × 2 cells large-amplitude (+5 %) high velocity anomaly to see how our parameterization and data set could recover such a structure (Fig. 7c). Secondly, by using two 2 × 2 cells large-amplitude (±5 %) high and low velocity anomalies beside each other we evaluated the capability of the data set to resolve the abrupt lateral change in velocity between the two anomalies (Fig. 7d). Based on these two synthetic data tests we conclude that within the region of highest resolution we may perfectly well resolve geometries and amplitudes of such features. Outside this region though the recovery is poor thus leading to differences in the geometries of the original and the recovered structure. The results also show a significant vertical leakage to the lower layer which should be considered in the interpretations.

Our data set contains a small number of possible explosions that may be badly located in depth due to significant epicentral distances to the nearest stations (Fig. 3). The resolution tests document, however, that these explosions do not significantly bias our tomographic result for this region.
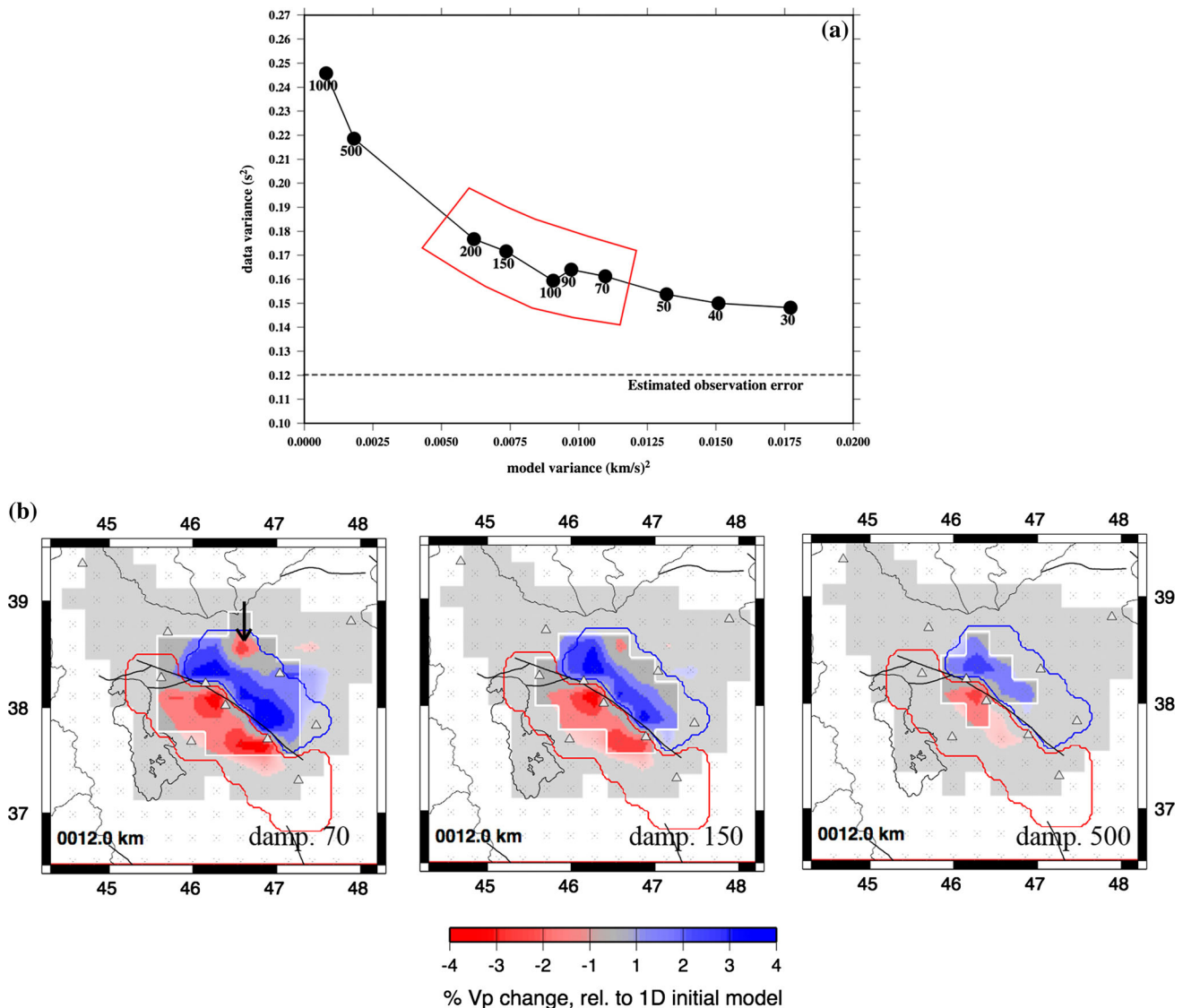
Fig. 5 Illustration of the valuation of appropriate damping. **a** *Trade-off curve* between data variance and model variance (Eberhart-Phillips 1986) for a solution after three iterations. The critical damping values are marked by a *red polygon*. *Dash line* delineates the estimated observation error level (0.12 s). **b** Characteristic synthetic data tests (Husen et al. 2000; Kissling 1988). The recovered model in the horizontal plane at 12 km is shown as obtained with different damping values of 70, 150 and 500. *Blue* and *red lines* denote positive and negative contrasts of ±5 % relative to the average layer velocity, respectively, and outline the velocity anomalies of the synthetic input model. *Grey triangles* display stations and *black solid lines* mark the faults. The *arrow* illustrates the artifact anomaly generated during the inversion. Areas in *white* are outside the ray coverage of the data set while areas marked in *bold color* and enclosed by *solid white line* are well resolved. In between area in *light grey* is poorly to fairly-well resolved (see the text for more details about resolution analysis)

4 Tomographic image of the 3D crustal structure

The new tomographic results (Figs. 6c, 8) provide new insight into the upper crustal structure around the NTF in the center of the study region. For the depth range between 6 km and 14 km, the resulting velocity model manifests two ∼60 km long anomalies with strong lateral velocity variations from 4 % higher than average in the SW to 4 % lower than average in the NE across a boundary paralleling the NTF surface expression (Fig. 6c). Below 14 km depth

the pattern remains the same as in the shallow layers though the region of highest resolution is too small to draw any conclusion on this. Our resolution tests document that geometry and velocity amplitude of anomalies at depth between 6 and 14 km are well resolved and reliable on the scale of 120 km, while the anomaly contrast across the NTF fault seems sharply imaged.

At 5 km of the uppermost crust, we observe a local high velocity anomaly (marked by a star in Fig. 6c), overlaying a regional low velocity anomaly north of the
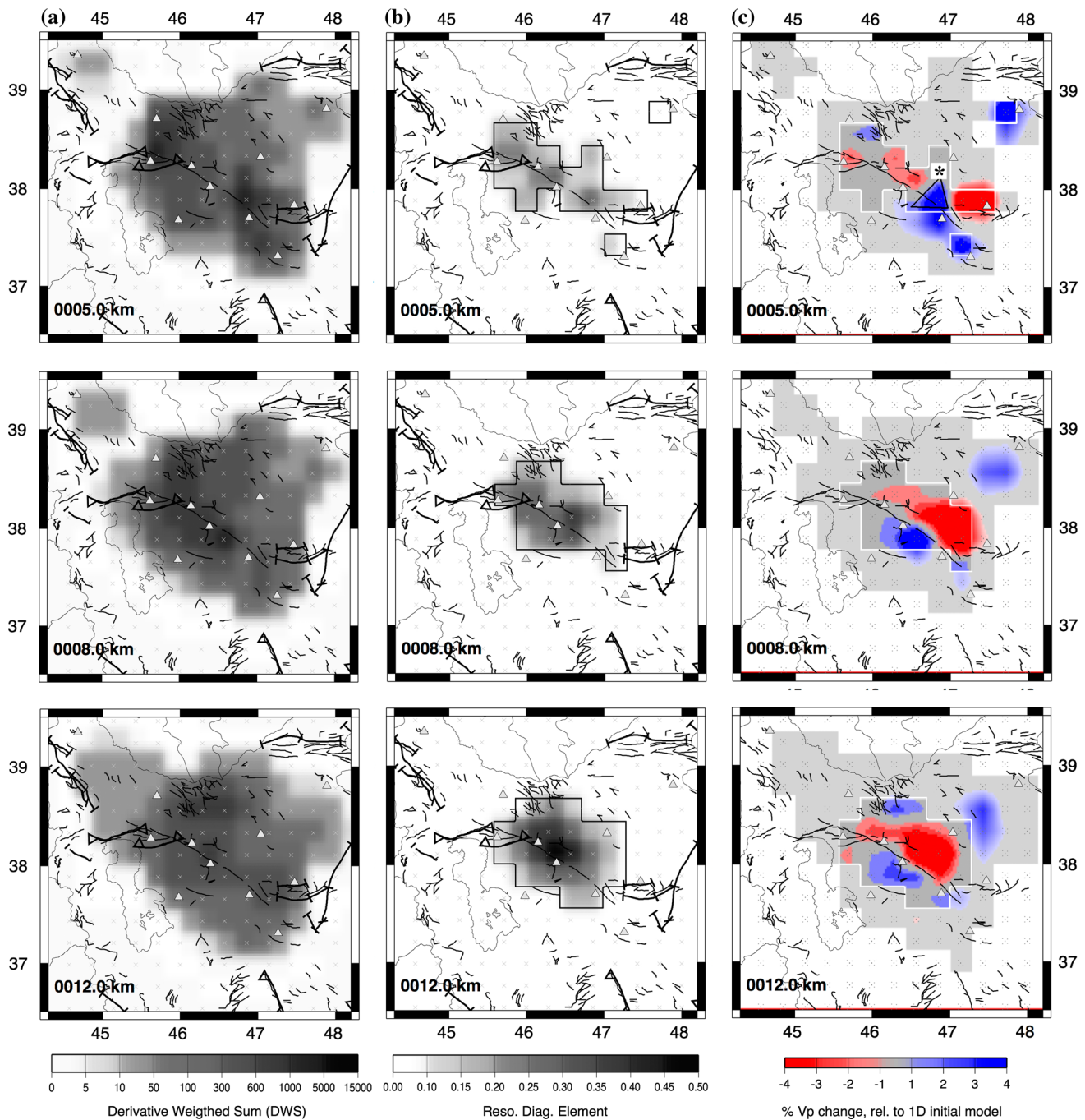
Fig. 6 a Derivative weight sum (DWS), **b** resolution diagonal elements (RDE) and **c** inversion results for horizontal sections at 5, 8, and 12 km. *Gray triangles* show stations and *black solid lines* show the surface trace of the fault. The best resolved region (RDE value >0.1) is *outlined with black* (**b**) and *white* (**c**) *polygons. Light gray area* in part (**c**) masks cells that are hit by rays. Note the local high velocity anomaly (*star*) in a depth of 5.0 km that extends across the NTF, whereas at 8.0 km and 12.0 km depth range this fault separates the high velocity on its southern side from the low velocity on its northern side

NTF of which we discussed its spatial resolution in the previous section (Figs. 7c, d). Our resolution tests also suggest that the anomalies at a depth of 5 km and shallower are locally influenced by leakage from deeper layers (Fig. 7a, b). Since vertical leakage as the cause of

a shallow local high velocity anomaly would not imply a regional high velocity anomaly overlying a regionally low velocity anomaly at depth, we conclude that this velocity structure at 5 km depth is real in amplitude sign.

% Vp change, rel. to 1D initial model
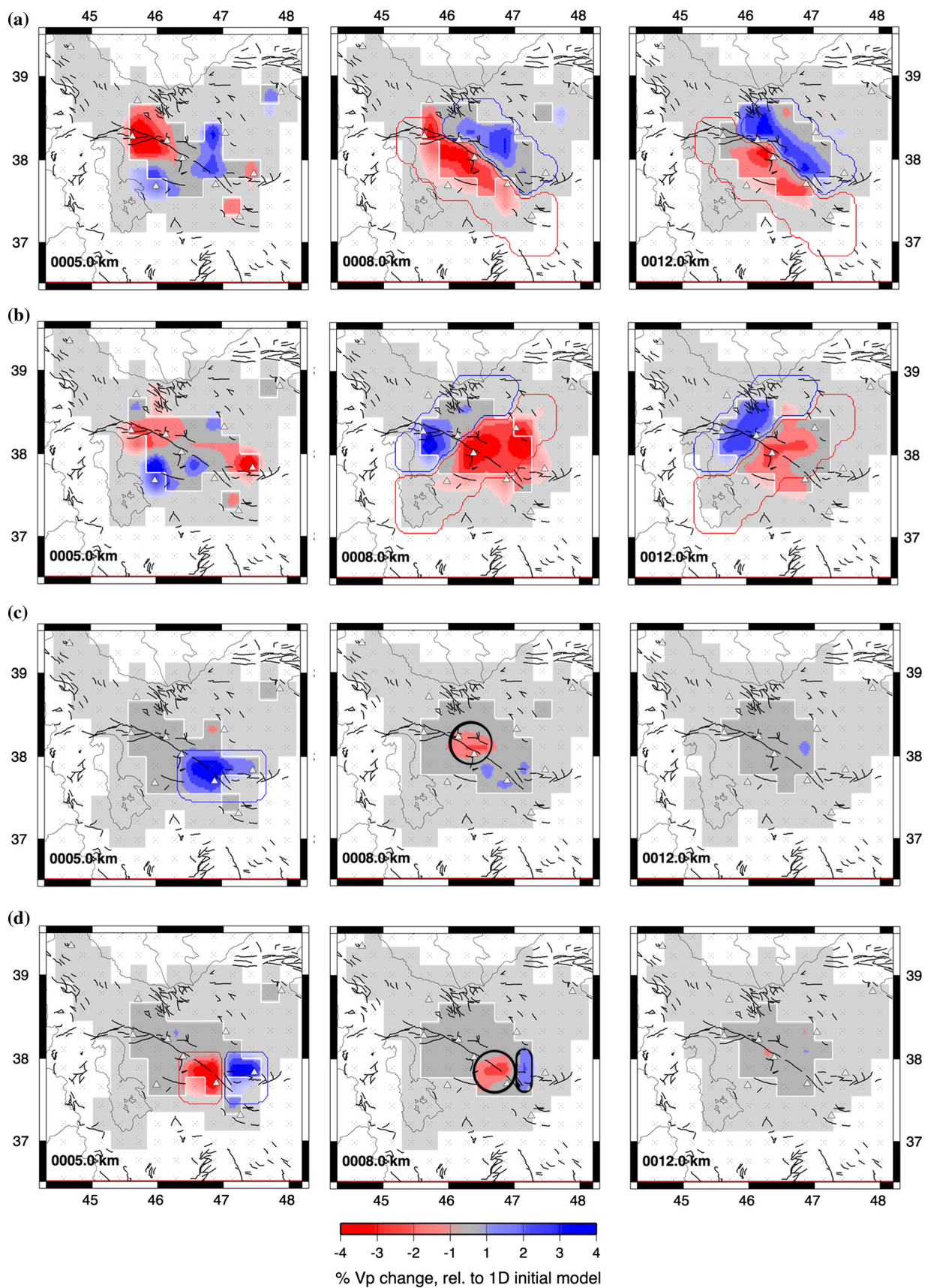
◄**Fig. 7** Test results obtained by inversion of synthetic data for four specifically designed models. **a** Results for a model with two anomalies of 5 % high and 5 % low amplitude paralleling on either side the NTF; **b** same as **a** but anomalies elongated in direction perpendicular to NTF; **c** a single 4 × 2 cells large anomaly (5 % velocity increase) crossing from region of highest resolution into poorly resolved region; **d** two 2 × 2 cells (one of 5 % increased and one of 5 % decreased velocity). In all cases, the input model is shown in *red* and/or *blue line* regard to its negative and positive contrast of 5 %, related to the initial 1D velocity model, respectively. *Gray triangles* show stations and *black solid lines* illustrate the faults strand; *White border* shows RDE line of 0.1 and *light gray area* masks cells which rays hit

For the uppermost layer (0.0 km depth), however, the region of highest resolution is confined to a few patches. The results display two large amplitude high and low velocity anomalies, respectively, south and north of the NTF (labeled 1a and 2 in Fig. 8G) in the regions with highest resolution, which are consistent with anomalies in the deeper layers. In addition, the local high velocity anomaly (labeled 1b in Fig. 8G) in the region with fairly good resolution, north of the NTF, corresponds well with the local anomaly at 5 km depth (marked by star in Fig. 6c).

Cross sections through the resulting 3D model manifest the regional trend of high velocity SW and low velocity NE of the NTF from surface to ∼14 km depth in the A, B, C and E sections, and from 6 km to 14 km depth in the D and F sections (Fig. 8). Our results show that the NTF consistently dips to the SW in 4 km to 14 km depth, separating a high velocity rock volume in the south from the low velocity rocks in the north. Our synthetic tests (Fig. 7c, d) document a well-resolved amplitude and geometry of the model in the D and F sections. Thus, we suggest in shallower depth (3–8 km) a realistic and sharply imaged high velocity anomaly overlaying a low velocity anomaly.

5 Discussion

Using local earthquake tomography of the recorded events by the permanent stations in NW Iran, we obtained new constraints on the 3D P-velocity structure of the upper crust along an about 120 km long section of the NTF. Our results illustrate the surface expression of the NTF as the boundary separating two rock volumes with significantly different P-velocities (8 % or more), down to at least 14 km depth. Considering that our absolute velocity minimum 1D model denotes just the average of two approximately equal sizes with negative and positive amplitude velocity anomalies, and considering the limited size of the region of highest resolution, the model could not clearly define the regional absolute velocity structure. Geologically, we associate the

high velocity anomaly (average velocity of 6.3 km/s with predominantly basic volcanic rocks (e.g., basalt) related to the Sahand volcano eruptions and the low velocity anomaly (average velocity of 5.8 km/s) with the thick Mesozoic to Quaternary sequence of sedimentary rocks (Aghazadeh et al. 2010; Haghipur and Aghanabati 1985).

Cross sections through the resulting 3D model illustrate the boundary between these regional velocity anomalies, consistent with location and strike of the NTF at shallow depth (Fig. 8). Though the resolution is limited down to 3 km depth, our results further show that along this 70 km sector of the NTF, the fault dip decreases abruptly at a depth of 6–10 km from near vertical to ∼60° toward the southwest, correlating well with the micro seismicity results presented by Moradi et al. (2011). The GPS studies (Copley and Jackson 2006; Djamour et al. 2011; Rastbood and Voosoghi 2011; Vernant et al. 2004) suggested that the northern side of the NTF (e.g., Talesh region) has a velocity vector of 14–16 mm/yr along 10°–20° while the southern side (e.g., Zagros mountain and Main Zagroz Thrust (MZT)) exhibits a velocity of 12–16 mm/year in the direction 340°–350° (Fig. 1). Therefore, differential movements of Zagros and Talesh crustal blocks (Fig. 1) document a normal faulting component in addition to the prominent strike-slip mechanism of the NTF. Furthermore, surface geomorphology (Fig. 9) shows a higher topography and uplift of the northern footwall of the NTF, versus the lower topography of the southern hangingwall of the NTF, which is dominated by the Sahand volcanism. Interestingly, the bending and/or stepping of the fault caused the local transtensional tectonic regimes along the fault strand, which manifests itself as normal faulting components in GPS studies (Fig. 2) and also by variation of the fault dip in our tomographic results (Fig. 8). Shahryar Solaymani Azad et al. (2015) documented occurrence of local thrust faulting due to transpressional regimes in the restraining bends or step-overs of the fault. Thus, variations in fault attitude at shallow depth are expected due to local extensional and compressional regimes along the NTF and possibly also as a result of temporal stress variations due to interferences between slip at various fault segments. This suggests the separation between two lithologies might not be bounded by one fault and it is possible to have several faults at the same place.

As shown in Fig. 8, for the cross sections A, B, E, and possibly, C the majority of well-locatable event clusters is fairly consistent with the fault projection to depth. In sections D and F, however, no direct relation between hypocenter location and velocity anomalies near the NTF does exist. Obviously, the number of events is too small to draw any precise conclusions.

Based on the 5 km map section (Fig. 6) and the cross sections D and F (Fig. 8), the high velocity anomaly that overlies the regional low velocity anomaly could be a thin
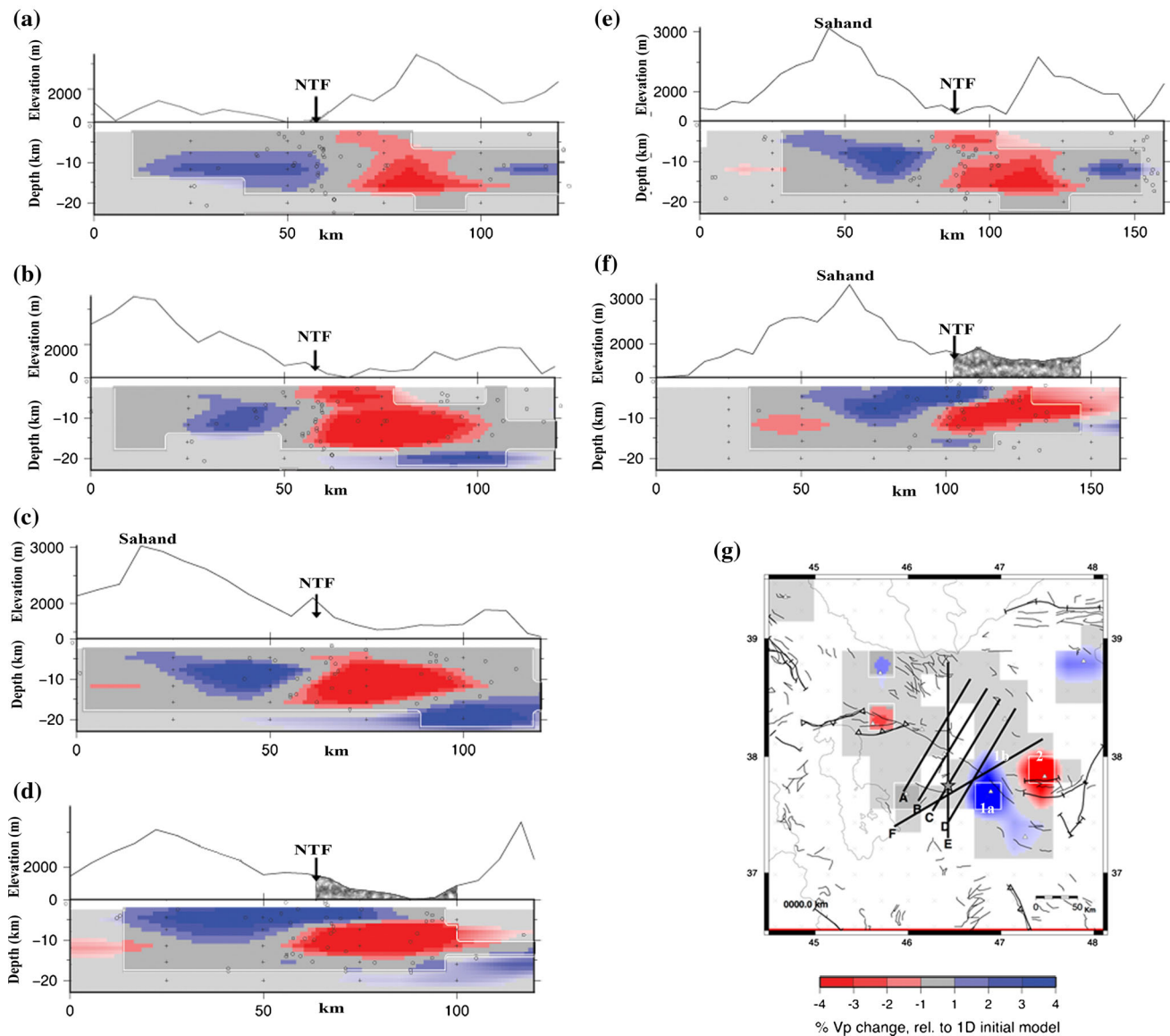
Fig. 8 In the vertical sections (**a–f**), *circles* manifest hypocenters of earthquakes; *White polygons* show the border of a RDE value of 0.1. Sahand shows the surface location of the Sahand volcano and the *arrow* with the NTF illustrates the surface expression of the North Tabriz Fault; *light gray area* masks cells which are hit by rays. We masked the 3 km *top layer* in all cross sections because our data could not solve this part of the area where the sections go across. The inset map (**g**) shows the surface (0.0 km depth) output map section with the position of *vertical slices* through areas of interest. The *star* shows the Sahand volcano. Labels 1a and 2 mark the well-resolved high- and low-velocity anomalies, respectively, while label 1b outlined by *blue dashed lines* denotes the fairly well resolved high-velocity anomaly. The areas marked in *grey* in cross sections **d** and **f** show surficial Pliocene-Quaternary sedimentary rocks, north of NTF

surface layer of volcanic rocks that at this location cross the fault strand and cover the sedimentary rocks in the north of NTF. As illustrated in Fig. 9, there is not much difference in surface geomorphology and mapped lithology around this overlaying anomaly (labeled 1b). Still, it is possible that this shallow high velocity anomaly represents a series of basaltic lava flows related to the earlier volcanic eruptions of the Sahand volcano that crossed the NTF and nowadays are buried beneath a few hundred meters of Plio-Quaternary sediments. Considering the recent tectonic

activity of the right-lateral strike-slip NTF, however, this would imply either relatively young Cenozoic eruption by Sahand volcano or by another yet unknown source.

6 Conclusion

We imaged the 3D crustal structure of the NW Alborz Mountain in a region that encompasses an about 120 km-long of the right-lateral strike-slip segment of the NTF. Our
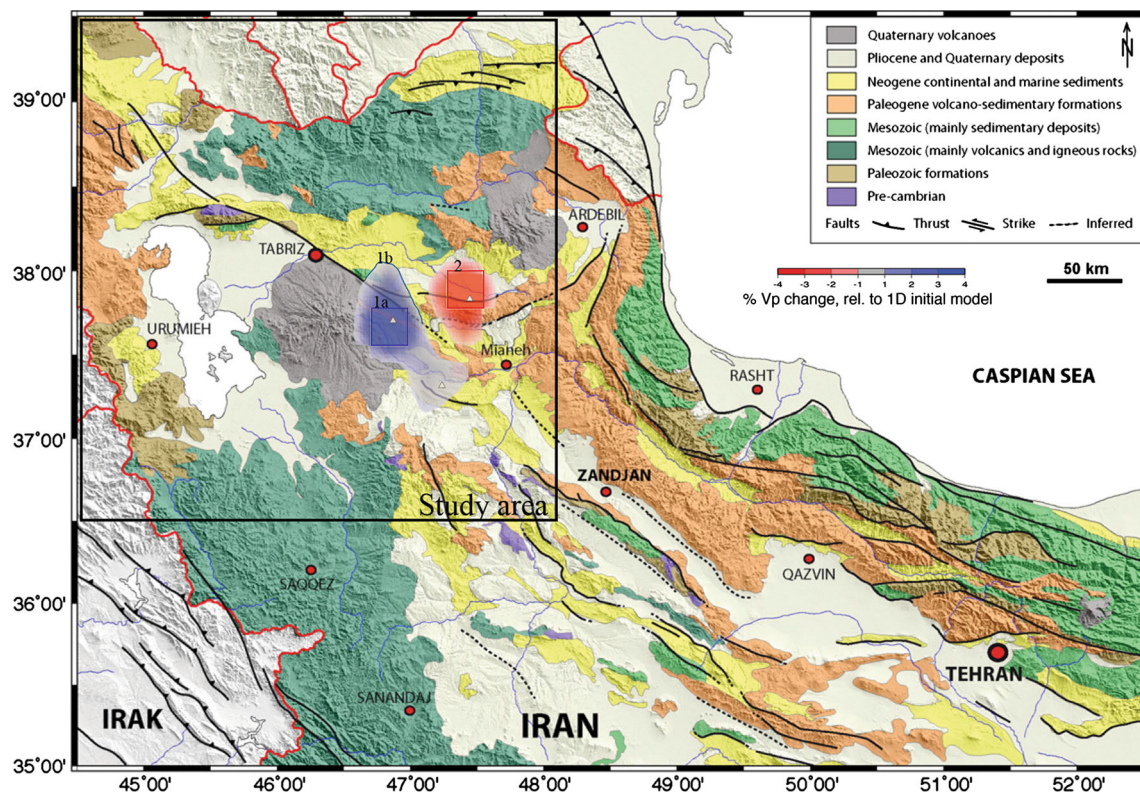
Fig. 9 Simplified geological map of NW Iran modified from Solaymani Azad et al. (2011), overlain by the shallow depth local velocity anomalies corresponding to Fig. 8G. Labels 1a and 2 mark the well-resolved high- and low-velocity anomalies, respectively, while label 1b marks the fairly-well resolved high-velocity anomaly (see text)

results show two high and low velocity anomalies in the upper crust, down to at least 14 km depth, with their boundaries parallel to the NTF surface expression. We interpret these velocity anomalies as basaltic volcanic rocks in the south and Mesozoic sedimentary and basement rocks north of the NTF. It is difficult to discuss about the lithology that we have in our interpretation, however, cross sections through the resulting 3D model display significant changes in dip of the NTF from a vertical attitude to ∼60° toward the southwest. At shallow depth (down to 5 km), a thin local high velocity rock volume extends across the NTF and overlies the regional low velocity layer north of the fault.

References

Aghazadeh, M., Castro, A., Omran, N. R., Emami, M. H., Moinvaziri, H., & Badrzadeh, Z. (2010). The gabbro (shoshonitic)–monzonite–granodiorite association of Khankandi pluton, Alborz Mountains, NW Iran. *Journal of Asian Earth Sciences, 38*(5), 199–219.

Ambraseys, N. N., & Melville, C. P. (1982). *A history of persian earthquakes*. New York: Cambridge University Press.

Azad, S. S., Dominguez, S., Philip, H., Hessami, K., Forutan, M., Shahpasandzadeh, M., & Ritz, J. F. (2011). The Zandjan fault system: morphological and tectonic evidences of a new active fault network in the NW of Iran. *Tectonophysics, 506*(1), 73–85.

Azad, S. S., Philip, H., Dominguez, S., Hessami, K., Shahpasandzadeh, M., Foroutan, M., et al. (2015). Paleoseismological and morphological evidence of slip rate variations along the North Tabriz fault (NW Iran). *Tectonophysics, 640*, 20–38.

Azizi, H., & Moinevaziri, H. (2009). Review of the tectonic setting of cretaceous to quaternary volcanism in northwestern Iran. *Journal of Geodynamics, 47*(4), 167–179.

Bayramnejad, E. (2007). Determination of crustal velocity structures in NW Alborz by using 3D local earthquake data inversion. *Ph.D. dissertation* (pp. 123). Tehran University, Tehran, Iran.

Berberian, M. (1976). Contribution to the seismotectonics of Iran (part II–III): In commemoration of the 50th anniversary of the Pahlavi dynasty (No. 39). *Ministry of Industry and Mines, Geological Survey of Iran, Tectonic and Seismotectonic Section*.

Berberian, M. (1997). Seismic sources of the Transcaucasian historical earthquakes. In D. Giardini & S. Balassanian (Eds.), *Historical and prehistorical earthquakes in the Caucasus* (pp. 233–311). Dordrecht: Kluwer Academic Publishers.

Copley, A., & Jackson, J. (2006). Active tectonics of the Turkish-Iranian Plateau. *Tectonics, 25*, TC6006.

Djamour, Y., Vernant, P., Nankali, H. R., & Tavakoli, F. (2011). NW Iran-eastern Turkey present-day kinematics: results from the

Iranian permanent GPS network. *Earth and Planetary Science Letters, 307*(1), 27–34.

Eberhart-Phillips, D. (1986). Three-dimensional velocity structure in northern California Coast Ranges from inversion of local earthquake arrival times. *Bulletin of the Seismological Society of America, 76*(4), 1025–1052.

Eberhart-Phillips, D. (1993). Local earthquake tomography: earthquake source regions. In H.M. Iyer & k. Hirahara (Eds.), *Seismic tomography: theory and practice* (pp. 614–643). London: Chapman and Hall.

Evans, J. R., Eberhart-Phillips, D., & Thurber, C. (1994). User's manual for simulps12 for imaging VP and VP/VS: a derivative of the Thurber tomographic inversion simul3 for local earthquakes and explosions. *US Geological Survey Open File Report OFR, 94–431*, 101.

Haghipur, A., & Aghanabati, A. (1985). Geological map of Iran. Based on available information of Geological Survey of Iran and National Iranian Oil Company for Zagros and Kopet Dagh regions. *Geological Survey of Iran*.

Haslinger, F., & Kissling, E. (2001). Investigating effects of 3-D ray tracing methods in local earthquake tomography. *Physics of the Earth and Planetary Interiors, 123*(2), 103–114.

Hessami, K., Pantosti, D., Tabassi, H., Shabanian, E., Abbassi, M.R., Feghhi, K., & Solaymani, S. (2003). Paleoearthquakes and slip rates of the North Tabriz Fault, NW Iran: preliminary results. *Annals of Geophysics*, [S.l.], *46*(5), ISSN 2037-416X.

Husen, S., Kissling, E., & Flueh, E. R. (2000). Local earthquake tomography of shallow subduction in north Chile- A combined onshore and offshore study. *Journal of Geophysical Research, 105*(B12), 28–183.

Jackson, J. (1992). Partitioning of strike-slip and convergent motion between Eurasia and Arabia in eastern Turkey and the Caucasus. *Journal of Geophysical Research: Solid Earth, 97*(B9), 12471–12479.

Kheirkhah, M., Allen, M., & Emami, M. (2009). Quaternary syn-collision magmatism from the Iran/Turkey borderlands. *Journal of Volcanology and Geothermal Research, 182*(1), 1–12.

Kissling, E. (1988). Geotomography with local earthquake data. *Reviews of Geophysics, 26*(4), 659–698.

Kissling, E., Ellsworth, W., Eberhart-Phillips, D., & Kradolfer, U. (1994). Initial reference models in local earthquake tomography.

Journal of Geophysical Research: Solid Earth, 99(B10), 19635–19646.

Kissling, E., Husen, S., & Haslinger, F. (2001). Model parametrization in seismic tomography: a choice of consequence for the solution quality. *Physics of the Earth and Planetary Interiors, 123*(2), 89–101.

Kissling, E., Kradolfer, U., & Maurer, H. (1995). *Program VELEST user's guide, short intrduction*. Zurich: Institute of Geophysics and Swiss Seismological Service, ETH.

Moradi, A. S., Hatzfeld, D., & Tatar, M. (2011). Microseismicity and seismotectonics of the North Tabriz fault (Iran). *Tectonophysics, 506*(1), 22–30.

Rastbood, A., & Voosoghi, B. (2011). Extension and slip rate partitioning in NW Iran constrained by GPS measurements. *Journal of Geodetic Science, 1*(4), 286–304.

Rizza, M., Vernant, P., Ritz, J., Peyret, M., Nankali, H., Nazari, H., et al. (2013). Morphotectonic and geodetic evidence for a constant slip-rate over the last 45 kyr along the Tabriz fault (Iran). *Geophysical Journal International, 193*(3), 1083–1094.

Taghizadeh-Farahmand, F., Sodoudi, F., Afsari, N., & Ghassemi, M. R. (2010). Lithospheric structure of NW Iran from P and S receiver functions. *Journal of Seismology, 14*(4), 823–836.

Thurber, C. (1993). Local earthquake tomography: velocities and Vp/Vs-theory. In H.M. Iyer & K. Hirahara (Eds.), *Seismic tomography: theory and practice* (pp. 563–583). London: Chapman and Hall.

Toomey, D., & Foulger, G. (1989). Tomographic inversion of local earthquake data from the Hengill-Grensdalur central volcano complex, Iceland. *Journal of Geophysical Research: Solid Earth, 94*(B12), 17497–17510.

Vernant, P., Nilforoushan, F., Hatzfeld, D., Abbassi, M., Vigny, C., Masson, F., et al. (2004). Present-day crustal deformation and plate kinematics in the Middle East constrained by GPS measurements in Iran and northern Oman. *Geophysical Journal International, 157*(1), 381–398.

Westaway, R. (1990). Seismicity and tectonic deformation rate in Soviet Armenia: implications for local earthquake hazard and evolution of adjacent regions. *Tectonics, 9*(3), 477–503.

Westaway, R. (1994). Present-day kinematics of the Middle East and eastern Mediterranean. *Journal of Geophysical Research: Solid Earth, 99*(B6), 12071–12090.